Available online at www.sciencedirect.com

ScienceDirect

Advances in Space Research xxx (xxxx) xxx

ADVANCES IN SPACE RESEARCH
(a COSPAR publication)

www.elsevier.com/locate/asr

Total ionising dose multilayer shielding optimisation for nanosatellites on geostationary transfer orbit

Anton Fetzer [a,*], Marius Anger [a], Philipp Oleynik [b], Jaan Praks [b]

[a] Department of Electronics and Nanoengineering, Aalto University, Maarintie 8, Espoo 02150, Finland
[b] Department of Physics and Astronomy, University of Turku, Vesilinnantie 5, Turku 20014, Finland

Received 16 June 2023; received in revised form 13 October 2023; accepted 17 October 2023

Abstract

The rising number of proposed nanosatellite missions with Commercial Off-The-Shelf electronics to higher orbits necessitates innovative, compact, and lightweight radiation shielding. In this study, several thousand multilayer radiation shielding configurations were simulated against trapped particle spectra predicted for a geostationary transfer orbit to demonstrate how material combinations and layer structures can be selected to minimise the total ionising dose inside nanosatellites with constrained mass budgets. The Geant4 Radiation Analysis for Space (GRAS) application was used to calculate ionising dose deposition behind multilayer shielding. Thousands of planar shielding stacks were procedurally generated and simulated on top of silicon plates representing sensitive semiconductor devices. To allow for comparison between configurations, all shielding stacks had a total mass of 1.5 g/cm^2, and shielding performance was evaluated based on the total ionising dose absorbed by the silicon plates. The simulations consistently show that configurations with low-atomic-number (low-Z) materials on top of high-Z materials yield the lowest doses. The two- and three-layer mass allocation optimisations demonstrate the non-linear dependence of ionising dose on mass allocation between materials. Optimised polyethylene-lead shields achieved up to 30% lower ionising doses compared to an equal mass of either of the two materials or up to 50% lower than the same mass of aluminium. Contrary to previous claims about Z-graded shielding, no significant improvements were observed for using more than two different materials, and optimisation of multilayer shields tends to reduce them to two-layer structures. Optimal multilayer radiation shielding depends on various factors and must be tailored to specific radiation environments and mission requirements. The primary contributions of this article are the methods presented for achieving this tailoring using open-source software and parallel computing. The multilayer simulations performed for this work resulted in an extensive dataset for multilayer shielding performance that enabled novel visualisations of the ionising dose dependence on shielding composition based on quantitative results.

Keywords: Radiation; Shielding; Van-Allen belts; Geant4; Multilayer; Optimisation; Small satellite; Nanosatellite; CubeSat; Ionising dose

1. Introduction

Concerns about radiation effects on space electronics have intensified as nanosatellite missions have evolved from low-Earth orbit (LEO) to high elliptical orbits (Blum et al., 2020) and interplanetary space (Freeman, 2020). LEO missions benefit from relatively benign radiation levels and new nanosatellite technology, enabled by affordable Commercial Off-the-Shelf (COTS) components (Samwel et al., 2019; Woellert et al., 2011). Space above LEO presents a radiation threat due to trapped charged particles in the Earth's magnetic field (Russell, 2000) and solar energetic particles (Mewaldt, 2007). The limited mass

---

* Corresponding author.
E-mail addresses: Anton.Fetzer@aalto.fi (A. Fetzer), Marius.Anger@aalto.fi (M. Anger), Philipp.Oleynik@utu.fi (P. Oleynik), Jaan.Praks@aalto.fi (J. Praks).

https://doi.org/10.1016/j.asr.2023.10.028
0273-1177/© 2023 COSPAR. Published by Elsevier B.V.

Please cite this article as: A. Fetzer, M. Anger, P. Oleynik et al., Total ionising dose multilayer shielding optimisation for nanosatellites on geostationary transfer orbit, Advances in Space Research, https://doi.org/10.1016/j.asr.2023.10.028

budgets of nanosatellites prevent the use of generous radiation shielding, necessitating innovative solutions. Despite these concerns, several CubeSat missions have been proposed to geostationary transfer orbit (GTO) (Madry and Pelton, 2020; Kopacz et al., 2020) or other high-radiation space environments: SpectroCube (Elsaesser et al., 2020), GTOSat (Blum et al., 2020), Orbital Factory II (Everett et al., 2018), and Shields-1 (Thomsen et al., 2015).

The near-Earth radiation environment comprises the Van Allen radiation belts, galactic cosmic rays, and solar energetic particles (Vainio et al., 2009). For all three radiation sources, models are available to predict the particle fluxes experienced by a satellite traversing the radiation environment (Ginet et al., 2013; Badhwar and O'Neill, 1996; Jiggens et al., 2014). The trapped particle spectra of the Van Allen belts are the most significant source of total ionising dose on GTO, as shown in Fig. 6, which is why they were chosen as the example environment to demonstrate the multilayer optimisation.

Without the ability to carry a heavy radiation shield for their electronics, CubeSat missions beyond LEO require innovative radiation mitigation strategies. Alternative materials can improve shielding performance (Emmanuel et al., 2014). Further improvements can be achieved by combining different materials into multilayer radiation shielding, which has been investigated since the 1940s (Sasse, 1965). However, which materials to combine to achieve minimal TID depends on the specific radiation environment (Arif Sazali et al., 2019).

Rohach reported in 1966 that encasing heavy materials with lighter ones achieves weight-efficient shielding (Rohach, 1966). Rossi and Stauber investigated the optimisation of two-layer shielding configurations for space applications using particle transport codes in 1977 (Rossi and Stauber, 1977). Two-layer optimisation against electron-bremsstrahlung was performed by Barnea et al. in 1987 (Barnea et al., 1987). Recently, attempts have been made to identify effective shielding for specific environments using the Monte Carlo N-Particle Transport Code (MCNP) and genetic algorithms to optimise multilayer shielding against gamma rays and neutrons for nuclear applications (Hu et al., 2008) as well as electron and proton spectra in low-Earth orbit (Daneshvar et al., 2021). Multilayer configurations have been constructed with foils and tested against electron beams (Ibarmia et al., 2013).

While ground-based accelerator tests with measurements in controlled laboratory environments are the only way to reach definite conclusions about radiation shielding performance, accelerator facilities cannot fully reproduce the broad particle spectra in space that span several orders of magnitude in energy (Emmanuel and Raghavan, 2016). Simulations are not limited in this way and allow arbitrary particle spectra to be simulated (Allison et al., 2016). Modern computing hardware, in combination with free, open-source simulation software, provides a fast and affordable alternative to estimate the performance of spacecraft radiation shielding.

The motivation for the presented simulations is the proposed Foresail-2 mission to geostationary transfer orbit (GTO), which intersects the most intense regions of the radiation belts (Anger et al., 2023; Anger et al., 2022). Despite the challenging radiation environment, Foresail-2 aims to use COTS electronic components, which sets ambitious requirements for the radiation shielding of the spacecraft.

The work presented in this article identified and optimised multilayer shielding configurations to minimise the total ionising dose received in a nanosatellite on orbit through the central regions of the Van Allen radiation belts. Several thousand multilayer configurations with up to five layers were simulated and analysed with publicly available open-source tools to identify suitable configurations that minimise the ionising dose received behind the shielding. Single-event effects and displacement damage are not discussed in this analysis, as these require different mitigation strategies that cannot be discussed in sufficient depth in the scope of this article (Winokur et al., 1999). The trapped particle spectra of the Van-Allen belts were used as an example environment, but the proposed multilayer optimisation can be performed for all particle species and energies that the Geant4 physics models cover.

The following Section 2 describes the methods and tools used for the ionising dose simulations. The results of the simulations are presented in Section 3, which also discusses the implications of the findings. Finally, Section 4 summarises the main conclusions of the article and provides recommendations for future work in radiation shielding optimisation for nanosatellites.

2. Total ionising dose simulation methods

The simulation approach for this study is outlined in Fig. 1. The first step is to model and estimate the particle spectrum for the orbit of the spacecraft. Several mathematical space radiation models are publicly available for this purpose. These models use historical data combined with physical relationships and assumptions to generate particle flux spectra along the orbit defined by the user (Rípa et al., 2020).

In the second step, a description of the geometries and materials with which the particles interact must be sup-

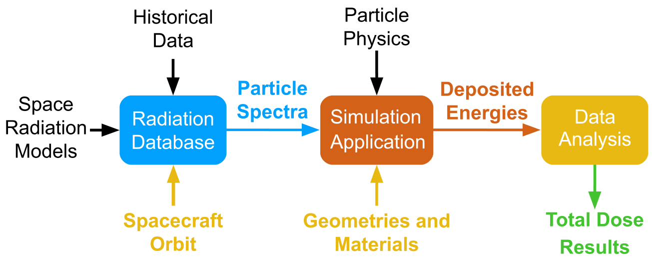

Fig. 1. Data- and workflow for space shielding simulations. The inputs in black are derived from published scientific data and models. User-specified inputs are marked in yellow, while the output is highlighted in green.

plied. To simulate the radiation interaction with the given materials and geometry, the particle simulation software generates a random sample of particles that follow the energy distribution of the input spectrum. These particles interact with the user-defined geometries and materials, depositing energies in the volumes of the simulated geometry according to the chosen physics models (Agostinelli et al., 2003). The energies deposited in detector volumes are summed up to calculate the Total Ionising Dose (TID) that would be received by sensitive components onboard the spacecraft.

In the third step, the TID values are further processed and visualised in their proper context, depending on the specific simulation.

2.1. Particle spectra estimation

The ESA Space Environment Information System (SPENVIS) (Heynderickx et al., 2000) was used to obtain the particle spectra for all simulations presented in this publication. SPENVIS provides standardised access to several recent space environment models through a user-friendly web interface (Heynderickx et al., 2004; Heynderickx et al., 2005). The trapped particles of the Van-Allen belts are the primary source of ionising dose on GTO, as shown in Fig. 6. It was therefore decided to use the trapped particle spectra as the example environment to demonstrate multilayer optimisation. As of 2023, the AP-9/AE-9 models are the de facto standard for calculating trapped electron and proton fluxes in Earth orbit (Ginet et al., 2013).

Table 1 shows the parameters used to generate the AP-9/AE-9 spectra using SPENVIS. The orbit is defined based on the launch date and perigee and apogee altitudes. Version 1.5 of the AP-9/AE-9 models was used in percentile mode with 97% confidence level. Only electrons above 500 keV and protons above 10 MeV deposit significant ionising doses behind 1 mm of aluminium shielding. Simulating particles with energies below these thresholds wastes computational resources, which is why the low-energy parts of the spectra were excluded from the simulations. The generated proton spectrum contained a trailing zero, which was removed to prevent issues with the power-law spectrum interpolation.

Table 1
Parameters used for the SPENVIS orbit generator and AP-9/AE-9 models on SPENVIS. The generated trajectory does not account for solar radiation pressure or atmospheric drag.

Parameter	Value
Orbit start	01. Jul. 2025 00:00:00
Trajectory duration	30 days
Perigee altitude	300 km
Apogee altitude	36000 km
Inclination	0°
Right Ascension of Ascending Node	0°
Argument of perigee	0°
True anomaly	0°
Particle models	AE9/AP9
Model version	1.5
Model run mode	percentile
Percentile	97%
Electron Energies	0.5 MeV to 10 MeV
Proton Energies	10 MeV to 1200 MeV
Interpolation type	power-law

Fig. 2 displays the expected average differential flux of protons and electrons, which would be received by a spacecraft on equatorial GTO according to AP-9/AE-9 with the parameters provided in Table 1.

For comparison, SEP spectra generated with the SAPPHIRE total fluence model (Jiggens et al., 2018) and GCR spectra from the ISO-15390 model (International Organization for Standardization, 2004) were also simulated. For both, the version provided by SPENVIS was used with the orbit parameters shown in Table 1. For SAPPHIRE, 97% confidence level was selected, while the ISO-15390 standard model was used in +2 Sigma mode. Both models generate flux spectra for ion species ranging from hydrogen to uranium. However, only some of the species contribute significantly to the total flux of solar and cosmic ions. To simplify the simulations only a selection of the most dominant species was simulated for each model. For SEPs, the chosen species were H, He, C, O, Ne, Mg, Si and Fe. For GCRs, the species H, He, C, N, O, Mg, Si and Fe were selected. The flux spectra of these ion species were simulated separately, and their deposited doses were summed to calculate the TID attributable to SEPs and GCRs. As shown in Fig. 6, their contribution to the TID received on GTO behind aluminium shielding is negligible compared to the TID due to trapped particles.

2.2. Particle-matter interaction simulation setup

The Geant4 Radiation Analysis for Space (GRAS) simulation application was used for this publication. GRAS is

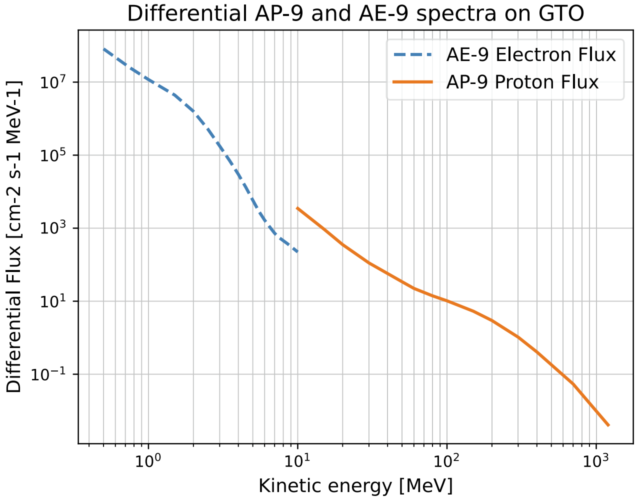

Fig. 2. Average differential flux spectra of trapped protons and electrons on GTO with 300 km perigee and 36 000 km apogee altitude, according to the AP-9/AE-9 models for trapped particle fluxes with 97% confidence level and other parameters as shown in Table 1 (Donder et al., 2018).

an executable software application for simulating space environment effects, based on the Geant4 toolkit (Santin et al., 2005) and was developed as a result of the European Space Agency's (ESA) involvement in the Geant4 collaboration (Lei et al., 2002). Geant4 is a Monte Carlo particle simulation toolkit for the passage of particles through matter and "incorporates a large part of all that is known about particle interactions" (Agostinelli et al., 2003, p. 253) (Allison et al., 2006; Allison et al., 2016; Geant4 Collaboration, 2022).

GRAS uses the physics and application libraries of Geant4 to provide a flexible application that can be controlled interactively or through macro files (Santin et al., 2005). The Geant4 default FTFP_BERT physics model was used for all simulations (Geant4 Collaboration, 2023a; Geant4 Collaboration, 2023b; Ivantchenko et al., 2012; Banerjee, 2012).

The particle simulations presented in this publication were performed using the processing power and data storage space of the Triton computing cluster provided by the Aalto University "Science-IT" project. The heterogeneous computing cluster consists of over 100 computing nodes with various multithreaded server CPUs, such as Xeon E5 2680 and Xeon Gold 6248. The cluster runs CentOS 7, with the SLURM scheduler and batch system (Aalto Science-IT, 2022). The GRAS simulation software and the Geant4 toolkit are platform-independent, which means the simulations could be performed on any computer, with the only difference being the run time. A trade-off between the computation time and the statistical significance of the results has to be made. The simulations presented in this publication were usually performed with more than 10^9 electrons and more than 10^7 protons each. In some cases, even higher numbers of particles were required to achieve acceptable statistics, with more than 10^{11} electrons simulated in a single run. The number of particles to be simulated was equally distributed across hundreds of GRAS instances, running in parallel on different threads of the computing cluster. Using this approach, most simulations were completed in under 12 h.

GRAS sums up the energies deposited by the particles and their secondary particles within the designated detector volumes of the simulation. Each GRAS instance generates a comma-separated values (CSV) file containing the energy deposited in each detector volume. The output can be expressed in MeV per simulated particle or in rad, which uses the GRAS internal analysis module, accounting for the detector volume, particle source surface area, and differential mission fluence. Python scripts were used to collect raw data from the output files of all GRAS instances, to process the data further, and to produce the visualisations presented in this publication.

GRAS produces all ionising dose results together with an estimate of the statistical error of the result. This error was considered and propagated through quadratic summation, assuming independent, normally distributed errors. The error contribution from the uncertainty in the particle spectra was neglected as the spectra are used merely as an example to demonstrate the optimisation methods under the assumption of a given particle environment. The systematic error of the FTFP_BERT Geant4 physics model cannot be directly quantified and was therefore also neglected. The uncertainties and errors for ionising dose values presented in all line plots and tables are therefore purely based on the statistical error of the Monte-Carlo simulation.

Before conducting the main simulations with Geant4 and GRAS, the setup and method were verified by comparing results with outputs from the SHIELDOSE-2Q tool for ionising dose estimates for simple geometries (Seltzer, 1980; Seltzer, 1994). SHIELDOSE-2Q calculates the ionising dose behind different thicknesses of simple shielding geometries containing a single material under irradiation from a given input particle spectrum. The SHIELDOSE-2Q implementation, available on SPENVIS, was used for this (Spenvis, 2018).

2.3. Simulation geometry setup

To optimise multilayer shielding, many shielding configurations must be simulated. The geometry of the configurations should therefore be simple to implement, replicable and fast to simulate. The planar geometry, as used by Emmanuel and Raghavan (2015), can be placed side by side in large numbers. It also ensures that all particles that traverse the shield will reach the detector volume. This makes efficient use of computational resources, maximising statistical accuracy.

Each multilayer configuration is implemented by stacking square shielding plates on top of one another, with a detector plate at the back, as shown in Fig. 3.

Shielding stacks consist of N material layers with thicknesses t_1 to t_N and corresponding layer depths d_1 to d_N. The total shielding depth is D in g/cm^2. The detectors are 0.5 mm thick silicon plates, representing the sensitive volumes of integrated semiconductor devices. The particles are generated on the surface of layer 1 with an inward-facing cosine angular distribution to represent the isotropic radiation environment of space. The energy distribution of the particles follows the input spectrum. The combination of a multilayer shielding stack and detector acts as the basic building block of the simulated geometries and is referred to as a shielding tile in the following.

The geometries for Geant4 simulations are implemented using the Geometry Description Markup Language (GDML)(Cern, 2020; Chytracek et al., 2006). It allows for text-based procedural generation of many radiation shielding tiles in a virtual three-dimensional world, as shown in Fig. 4.

In Fig. 4, the layer thicknesses are exaggerated to make the layer structure visible. To reduce effects on the edges of the tiles, sufficiently large tiles are needed compared to the few mm thick layers. In the actual simulations, the tiles

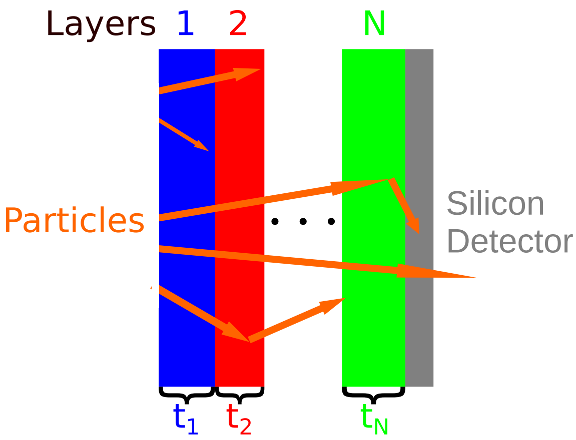

Fig. 3. Geometry of a planar multilayer shielding configuration with shielding layers and detector. The shielding stack has N layers, each with their respective thicknesses t_1 to t_N. The particles are generated on the surface of layer 1 with a cosine angular distribution, and the detector is placed at the back of layer N. Any energy deposited by the particles or their secondary particles in the silicon detector is registered and used to calculate the TID result of the simulation.

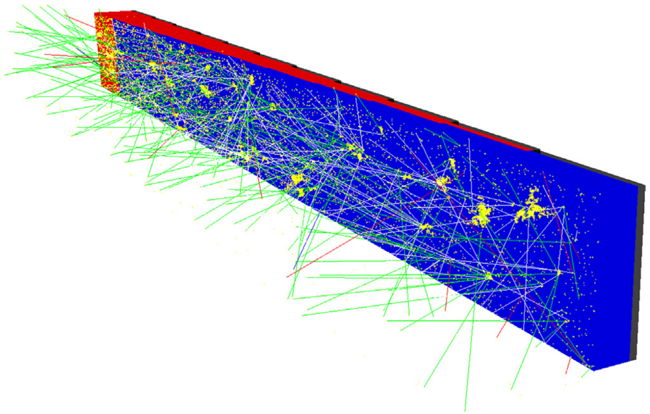

Fig. 4. Render of procedurally generated two-layer shielding tiles placed side by side. The particle tracks were simulated with Geant4. The thickness of the layers was increased for this visualisation to make the layer structure visible. The red and blue layers are shielding materials, and the grey layers are detector volumes.

measure 10 m by 10 m and are up to several millimetres deep. The silicon detector plates behind the shields are 0.5 mm thick.

As illustrated in Fig. 3, the blue and red layers represent two different shielding materials, while the grey layer at the back is a silicon plate that acts as the particle detector. The tiles are placed side by side such that their top layers form a smooth surface. Electrons and protons are generated at random locations on this surface, with each tile receiving an even share of the simulated particles. The number of particles must be sufficiently large to achieve statistical significance. This must be considered in the trade-off between computational time and statistical uncertainty in the results. The computation time also depends on the number of tiles. A significant increase in computation time was observed for simulations with over 1000 tiles, which is why most simulations were limited to this number.

2.4. Material permutations

A multilayer configuration is defined by its materials, the order in which they are arranged and the thicknesses $t_{1..N}$ or depths $d_{1..N}$ of each layer. This leads to an infinite number of possible configurations P even if the number of layers N and the number of possible materials M are limited. A systematic approach is needed to investigate this parameter space. Effective multilayer material combinations can be identified by simulating all permutations of a list of materials for a specified number of layers. The depth of the layers must be fixed to the same value to reduce the number of possible configurations to a finite value and to allow for comparison between configurations. Once a suitable selection and order of materials are found, the depth ratio between the layers can be further optimised.

Geant4 allows the procedural generation of large numbers of multilayer configurations through GDML scripts, as shown in Fig. 4. If M is the number of possible materials and N the number of layers, then the number of possible material permutations P in the multilayer stack is

$$P = M^N. \tag{1}$$

To be able to compare the different configurations, the thicknesses t_N of the layers are calculated from the densities of the materials ρ_N. This ensures that all layers have the same depth $d_{1..N} = d = D/N$ in g/cm^2. Consequently

$$t_N = \frac{D}{\rho_N \cdot N} = \frac{d}{\rho_N}. \tag{2}$$

Due to the different ρ_N of the materials, the actual $t_{1..N}$ can vary significantly despite having the same depth.

2.5. Two-layer mass allocation optimisation

The permutation simulations introduced in 2.4 allocate a fixed ratio of the shielding mass to each layer. However, the shielding performance can be further improved by optimising the mass ratio assigned to the different layers. To allow for a fair comparison between different configurations, all tiles must have the same total shielding depth D, which is defined as

$$D = \sum_{n=1}^{N} d_n = \sum_{n=1}^{N} (t_n \cdot \rho_n). \tag{3}$$

An example of such a configuration is shown in Fig. 4. The thicknesses t_1 and t_2 are calculated based on their position x, which enumerates the tiles from left to right with X being the number of tiles and $x \in 0, .., X-1$, therefore

$$t_1 = \frac{D}{\rho_1} \cdot \left(1 - \frac{x}{X-1}\right), \tag{4}$$

$$t_2 = \frac{D}{\rho_2} \cdot \frac{x}{X-1}. \tag{5}$$

Eqs. 4 and 5 ensure that the total shielding depth of the stack is equal to D, while the mass allocation between the two shielding materials changes linearly with increasing x. The leftmost tile only consists of layer one, and the rightmost tile only of layer two. The example geometry in Fig. 4 was generated with $X = 11$ such that the mass allocation between the two layers changes in steps of 10% between the tiles. The first tile is 100% layer 1, the second tile is 90% layer 1 and 10% layer 2, etc. The two-layer optimisation simulations presented in 3.3.1 were performed with $X = 101$ tiles to provide more granular results. Fig. 10 shows the results of such a two-layer optimisation.

2.6. Three-layer mass allocation optimisation

The same concept can be extended for three materials by adding a second gradient. To allow for direct comparison, the total depth of each shielding configuration must be the same. Three-layer optimisation can be visualised as ternary plots, as demonstrated by Alfred F. Rohach in 1967 (Rohach, 1966). The simulation geometry was implemented in GDML as a planar triangle comprised of 900 triangular tiles, where $L = 30$ is the total number of tiles along one side of the equilateral triangle as in Fig. 5. Each tile has three shielding layers and one detector layer. The total depth of the three layers adds up to 1.5 g/cm^2, and the detectors are 0.5 mm thick silicon plates.

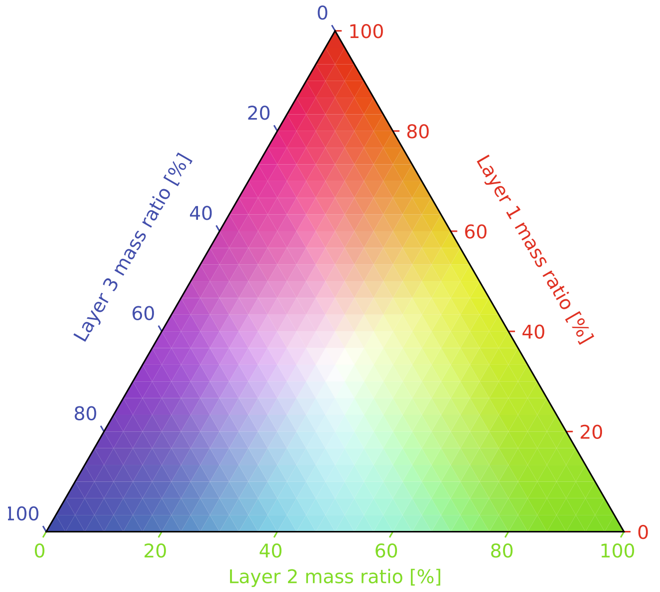

Fig. 5. Ternary plot illustrating the material allocation of the 900 triangular tiles, coloured according to their composition as RGB values. The top corner tile contains only material one, the lower right corner only material two, and the lower left corner only material three. The tiles in between contain combinations of the three layers according to their coordinates in the ternary plane. In the centre, the three layers have equal mass contributions, represented by the RGB values combining to white.

In the triangular grid, x and y represent the coordinates of a tile along the two sides of the equilateral triangle. For a given x, the value of y starts from 0 and goes up to $L - x - 1$. This constraint ensures the tiles are placed within the equilateral triangle, forming a grid that respects the triangular shape. The upward- and downward-pointing triangles are calculated separately to form a coherent grid without gaps and the layer thicknesses are calculated depending on their location in the triangle.

For upward-pointing triangles

$$t_A^{\uparrow} = \frac{D}{\rho_A} \cdot \left(1 - \frac{x}{L-1} - \frac{y}{L-1}\right), \tag{6}$$

$$t_B^{\uparrow} = \frac{D}{\rho_B} \cdot \frac{x}{L-1}, \tag{7}$$

$$t_C^{\uparrow} = \frac{D}{\rho_C} \cdot \frac{y}{L-1}, \tag{8}$$

while for the downward-pointing triangles

$$t_A^{\downarrow} = \frac{D}{\rho_A} \cdot \left(1 - \frac{x+1/3}{L-1} - \frac{y+1/3}{L-1}\right), \tag{9}$$

$$t_B^{\downarrow} = \frac{D}{\rho_B} \cdot \frac{x+1/3}{L-1}, \tag{10}$$

$$t_C^{\downarrow} = \frac{D}{\rho_C} \cdot \frac{y+1/3}{L-1}, \tag{11}$$

where $t_A^{\uparrow}, t_B^{\uparrow}, t_C^{\uparrow}, t_A^{\downarrow}, t_B^{\downarrow}$, and $t_C^{\downarrow}$ are the layer thicknesses of materials A, B, and C in upward and downward pointing triangles. The terms ρ_A, ρ_B, and ρ_C represent the respective densities, while D is the total shielding depth. The thicknesses vary depending on the position (x, y) of the tile within the equilateral triangle, ensuring a discrete gradient of the material allocation.

3. Results and discussion

3.1. Simulation setup verification

To validate the GRAS/Geant4 simulation setup, a comparison with the SHIELDOSE-2Q tool on SPENVIS was performed as introduced in Section 2.2. Fig. 6 shows the results of simulating 4.6×10^8 electrons and 9.7×10^8 protons with GRAS/Geant4 to produce ionising dose data with low statistical uncertainty. Between 0.5 g/cm^2 and 1.5 g/cm^2, the results from Geant4 and SHIELDOSE-2Q agree up to a few percent deviation, which validates the simulation setup. The target ionising dose rate to which the spacecraft should be shielded was chosen to be 1 krad per month to allow for a mission duration of up to one year using COTS electronic components. Geant4 and SHIELDOSE-2Q agree that 1.5 g/cm^2 are sufficient to reduce the expected TID to 1 krad per month assuming

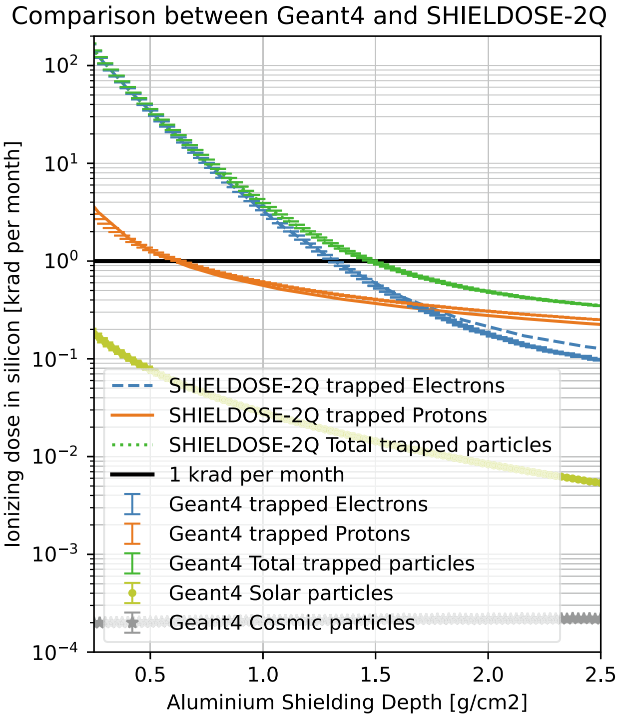

Fig. 6. Comparison between ionising dose results from simulations with Geant4 and SHIELDOSE-2Q. The two software agree that 1.5 g/cm^2 of aluminium shielding are sufficient to reduce the expected TID to 1 krad per month assuming the particle spectra shown in Fig. 2. TID results for solar particles and cosmic particles were added for comparison.

the particle spectra introduced in Section 2.1. All following simulations have been performed with 1.5 g/cm^2 of total shielding depth to allow for direct comparison between different configurations.

Fig. 6 also shows TID results for solar and cosmic particles on the GTO specified in Table 1. The dose contribution of the solar and cosmic particles is negligible compared to the trapped particles, and all following simulations were only performed with the trapped particle spectra.

The selected Geant4 default FTFP_BERT physics list was further validated by comparison with other Geant4 physics lists. For this purpose, the two-layer optimisation for polyethylene on top of lead (Fig. 10) was also performed with the other Geant4 reference physics lists QBBC, QGSP_BERT and QGSP_BIC as well as the electromagnetic physics options EM Opt3, EM Opt4 and EM Livermore. The maximum relative deviation between the dose values generated by the different models was less than 1.5% for both electrons and protons, which supports the validity of the results generated with the FTFP_BERT model.

3.2. Shielding stack material permutations

As introduced in Section 2.4, suitable material combinations can be found by simulating all possible layer permutations of a selection of materials arranged in a finite number of layers. To limit the number of possible permutations, equal mass was assigned to each layer. This also compensates for the different densities of the materials but requires further optimisation once suitable material combinations are found.

3.2.1. Single-layer shielding

To get a first understanding of the shielding performance of different materials, all chemical elements from hydrogen with Z-number 1 up to californium with Z-number 98 were simulated in planar slabs on top of 0.5 mm thick silicon detector plates as introduced in Section 2.3 with each of the shielding plates weighing 1.5 g/cm^2.

Fig. 7 shows the excellent shielding properties of hydrogen against both electrons and protons. The dose due to protons increases with the Z-number of the shielding material, while the dose due to electrons decreases for higher Z-numbers. The explanations for this behaviour are outside the scope of this study but can be found in literature such as the Review of Particle Physics chapter 34 (Workman et al., 2022). The simulation was performed with 4.3×10^{10} electrons and 1×10^8 protons, which results in statistical uncertainties below 0.5%. This is why the error bars of the data points are too small to be visible in the plot. Therefore, the fluctuations around the trend in Fig. 7 are not statistical fluctuations but represent differences in the simulated shielding performance between the materials. All simulation results contain systematic errors due to the physics model or the imperfect implementation of the materials, but these could not be quantified without physical measurements.

3.2.2. Two-layer permutations

The simulation of Section 3.2.1 was extended to two shielding plates on top of each other, with each of the

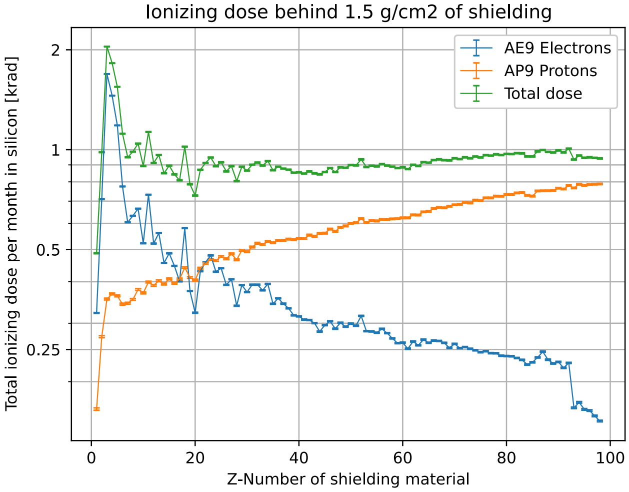

Fig. 7. Ionising dose deposited by the trapped particle spectra in 0.5 mm silicon behind 1.5 g/cm^2 shielding consisting of the first 98 chemical elements. High-Z materials shield well against electrons, while low-Z materials shield well against protons. The full dataset is publicly available on Zenodo (Fetzer, 2023a).

shielding plates weighing 0.75 g/cm^2 for a total of 1.5 g/cm^2. With 98 chemical elements in the database, there would be 9604 possible combinations, which slowed down the simulation significantly. The two-layer simulation was therefore performed for only the first 50 elements, which gives 2500 combinations. The full ionising dose results of this simulation for all 2500 combinations are published on Zenodo (Fetzer, 2023e).

Both Figs. 8 and 9 show the good shielding performance of hydrogen. Shielding combinations with lithium, beryllium, and boron perform significantly below average against electrons, while they do not stand out in the proton dose map. The performance differences between materials with high Z-numbers are minor, which gives the upper right quarter of the plots a uniform appearance. The proton map appears almost symmetrical along the diagonal from lower left to upper right. The electron map shows a slight gradient from the upper left to the lower right, indicating that low-Z combinations on top of high-Z materials generally perform better than high-Z materials on top of low-Z when shielding against trapped electrons.

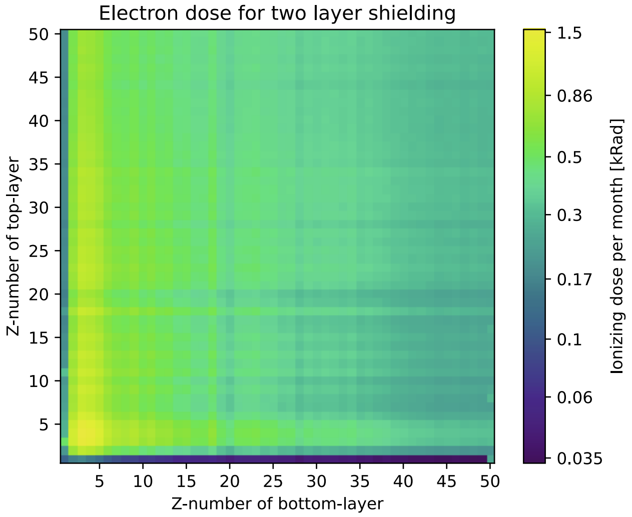

Fig. 8. Ionising dose deposited by trapped electrons in 0.5 mm silicon detectors behind shielding configurations consisting of all possible two-layer combinations of the first 50 chemical elements with each of the layers weighing 0.75g/cm^2 for a total of 1.5 g/cm^2 (Fetzer, 2023e).

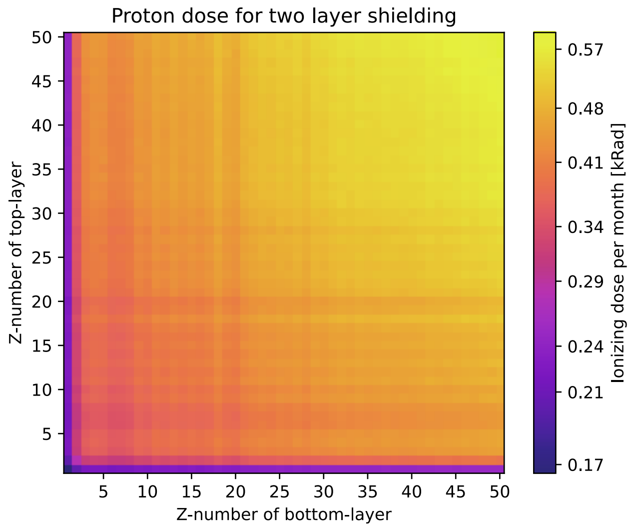

Fig. 9. Ionising dose deposited by trapped protons in 0.5 mm silicon detectors behind shielding configurations consisting of all possible two-layer combinations of the first 50 chemical elements with each of the layers weighing 0.75 g/cm^2 for a total of 1.5 g/cm^2 (Fetzer, 2023e).

3.2.3. Three-layer permutations

With three layers, the number of materials had to be reduced significantly to keep the total number of combinations low enough to run the simulation in a reasonable amount of time. It was decided to simulate only a selected list of ten materials that are commonly used in the aerospace industry or general radiation shielding, instead of chemical elements. If not otherwise specified, the material implementations in Geant4 were taken from the Geant4 material database (Geant4 Collaboration, 2021). The CubeSat standard specifies the aluminium alloys 7075, 6061, 5005 and 5052 to be used in CubeSats (The CubeSat Program, 2022). Alloy 6061 is more than 95% aluminium (The Aluminum Association, 2018) and is represented by elemental aluminium in the simulation. The aluminium alloy 7075 is up to 6.1% zinc, 2.9% magnesium and 2% copper, with other elements contributing less than one percent (The Aluminum Association, 2018) and the alloy was implemented with these mass percentages. Polyethylene and Kevlar have been investigated on the International Space Station as shielding materials (Narici et al., 2017). Kevlar is simulated as the pure material itself, as implemented in the Geant4 material database and not as a composite material. Lead is a common shielding material for ground-based radiation shielding and has been investigated for use in multilayer shielding systems (Arif Sazali et al., 2019). Tungsten has been proposed as part of a composite or multilayer shielding for space applications (Klamm, 2015). Stainless steel has been proposed as a spacecraft material by SpaceX (Scoles, 2022). The stainless steel implemented in the Geant4 database is 304 steel with 18% chromium and 8% nickel (Geant4 Collaboration, 2021). CubeSats contain significant amounts of printed circuit boards, which are usually made from FR4. Spacecraft structures can nowadays also be made from carbon fibres (Martins et al., 2018). The FR4 and carbon fibre implementations used in the simulations for this publication are taken from source code of Andrii Tykhonov (Tykhonov, 2019). Tantalum is used on a shielded satellite to GTO (Lucas et al., 2022). Teflon is used in space applications due to its low friction and high durability (Rutledge et al., 2001). Titanium is commonly associated with aerospace engineering, and the alloy Ti-6AL-4 V with 6% aluminium and 4% vanadium was chosen to represent common titanium alloys (Kumar et al., 2021).

Table 2 shows that multilayer configurations with polyethylene in the upper layer perform well against trapped protons and electrons when combined with high-Z materials like lead, tantalum or tungsten, which seem to be interchangeable as material for the bottom layer. Kevlar, a carbon-based low-Z material, performs slightly worse than polyethylene and is the only other material that appears in the middle and top layers of the five highest-ranked results. The five configurations that achieved the lowest TID values all have a high-Z material as their bottom layer. The configuration only containing the common spacecraft structure material Al-7075 performs poorly and ranks in the bottom 20%. The five combinations that resulted in the highest TIDs from this set all contain Teflon. The shield containing only Teflon resulted in more than twice the TID of the best-performing combination.

3.2.4. Four-layer permutations

With four layers, the number of materials had to be further reduced to only six, which gives a total of 1296 combinations. The materials were selected from the best performing materials of the three-layer simulation and are the aluminium alloy Al-7075, polyethylene, Kevlar, tungsten, stainless steel and FR4. All were implemented as explained in Section 3.2.3. The material lead was disqualified due to its weak structural integrity and toxicity. Tantalum was removed because it is interchangeable with tungsten. Due to their poor performance, carbon fibre, Teflon and titanium were removed from the material selection.

The top five best-performing four-layer shielding configurations of Table 3 all contain polyethylene in at least one of the two top layers or both of the upper layers, while all of them have tungsten as their bottom layer. As already seen in the three-layer results, Kevlar can replace individual layers of polyethylene but appears to perform slightly worse. The aluminium alloy that was part of the material list does not appear at all in the five best configurations but several times in the five worst combinations. Kevlar behind Aluminium seems to be a particularly bad radiation shield, with the worst-performing combination being steel on top of aluminium on Kevlar.

3.2.5. Five-layer permutations

A final fifth layer was added to the permutation simulation to allow for further optimisation. The material selection was reduced to only four to keep the number of possible combinations at 1024. For this, Kevlar and stainless steel were removed, and the simulation was performed with the following materials: polyethylene, tungsten, FR4 and Al-7075.

The five best results of the five-layer simulation shown in Table 4 all contain polyethylene in both top layers. The best results contain tungsten in their bottom layer, which further corroborates the claim that combinations of low-Z materials on top of high-Z materials tend to produce effective shields against the particle spectra of the radiation belts.

All five of the worst results contain tungsten in the outermost layer. Amongst this narrow selection of materials, the aluminium alloy performed particularly poorly, appearing 13 times in the worst five configurations.

Comparing the total dose values of the Tables 2–4 shows no significant reduction in TID when adding more layers. In Table 4, the two best results of all simulated five-layer configurations only contain two actual layers because neighbouring layers of the same material can be seen as one layer. Of the ten best five-layer configurations, none is a proper five-layer configuration. The best three-layer configurations generated in this simulation performed just as well as the best four-layer and five-layer configurations.

3.3. Layer mass allocation optimisation

Once suitable material combinations are identified, the shielding performance can be further optimised by varying the mass allocation between the layers as introduced in Sec-

Table 2
The three-layer shielding material combinations, which resulted in the lowest and highest TID of a total of 1728 simulated combinations of twelve different materials against the trapped electron and proton spectra. The aluminium alloy Al-7075 was included as a reference. Each of the layers has a depth of $0.5 g/cm^2$ for a total shielding depth of $1.5 g/cm^2$. The combinations are sorted and ranked according to their total dose shielding performance and presented with their statistical error. The full dataset with all 1728 combinations is publicly available on Zenodo (Fetzer, 2023d).

	Shielding Layers			Ionising dose [krad]		
Rank	**A**	**B**	**C**	**Electrons**	**Protons**	**Total Dose**
1	PE	PE	Pb	0.135 ± 0.004	0.3703 ± 0.0015	0.506 ± 0.004
2	PE	PE	Ta	0.145 ± 0.004	0.3654 ± 0.0014	0.511 ± 0.004
3	PE	PE	W	0.15 ± 0.004	0.3679 ± 0.0015	0.518 ± 0.004
4	PE	Kevlar	Pb	0.156 ± 0.004	0.3857 ± 0.0015	0.541 ± 0.004
5	Kevlar	PE	Pb	0.157 ± 0.004	0.3859 ± 0.0015	0.542 ± 0.004
...	...	...	...	...	...	...
1482	Al-7075	Al-7075	Al-7075	0.53 ± 0.007	0.4091 ± 0.0014	0.939 ± 0.007
...	...	...	...	...	...	...
1724	Teflon	Teflon	Carbon fibre	0.728 ± 0.007	0.3537 ± 0.0015	1.082 ± 0.008
1725	Al-7075	Teflon	Teflon	0.711 ± 0.008	0.3804 ± 0.0015	1.092 ± 0.008
1726	Ti_6AL_4V	Teflon	Teflon	0.711 ± 0.008	0.3885 ± 0.0015	1.099 ± 0.008
1727	Al-6061	Teflon	Teflon	0.726 ± 0.008	0.3792 ± 0.0014	1.105 ± 0.008
1728	Teflon	Teflon	Teflon	0.744 ± 0.007	0.3688 ± 0.0015	1.113 ± 0.008

Table 3
The four-layer shielding material combinations which resulted in the lowest and highest TID of a total of 1296 simulated combinations of six different materials against the trapped electron and proton spectra. The aluminium alloy Al-7075 was included as a reference. Each of the layers has a depth of 0.375g/cm^2 for a total shielding depth of 1.5g/cm^2. The combinations are sorted and ranked according to their total dose shielding performance and presented with their statistical error. The full dataset with all 1296 combinations is publicly available on Zenodo (Fetzer, 2023c).

	Shielding Layers				**Ionising dose [krad]**		
Rank	**A**	**B**	**C**	**D**	**Electrons**	**Protons**	**Total Dose**
1	PE	PE	PE	W	0.1639 ± 0.0027	0.3465 ± 0.0013	0.5103 ± 0.003
2	PE	PE	Kevlar	W	0.1805 ± 0.0029	0.3576 ± 0.0014	0.5381 ± 0.0032
3	PE	Kevlar	PE	W	0.1816 ± 0.0029	0.3581 ± 0.0013	0.5396 ± 0.0031
4	PE	PE	W	W	0.1257 ± 0.0023	0.4143 ± 0.0014	0.54 ± 0.0028
5	PE	PE	FR4	W	0.1733 ± 0.0028	0.3701 ± 0.0014	0.5434 ± 0.0031
...	...	...	...	...	...	...	...
1265	Al-7075	Al-7075	Al-7075	Al-7075	0.525 ± 0.004	0.4078 ± 0.001	0.933 ± 0.005
...	...	...	...	...	...	...	...
1292	Al-7075	Al-7075	Kevlar	Kevlar	0.613 ± 0.005	0.3573 ± 0.001	0.97 ± 0.005
1293	W	Al-7075	Al-7075	Al-7075	0.518 ± 0.004	0.4515 ± 0.002	0.97 ± 0.005
1294	Al-7075	Kevlar	Kevlar	Kevlar	0.633 ± 0.005	0.3411 ± 0.001	0.974 ± 0.005
1295	Steel	Al-7075	Kevlar	Kevlar	0.611 ± 0.005	0.3665 ± 0.001	0.978 ± 0.005
1296	Steel	Al-7075	Al-7075	Kevlar	0.595 ± 0.005	0.3888 ± 0.001	0.984 ± 0.005

Table 4
The five-layer shielding material combinations that resulted in the lowest and highest TID of 1024 simulated combinations of four different materials against the trapped electron and proton spectra. The aluminium alloy Al-7075 was included as a reference. Each of the layers has a depth of 0.3g/cm^2 for a total shielding depth of 1.5g/cm^2. The combinations are sorted and ranked according to their total dose shielding performance and presented with their statistical error. The full dataset with all 1024 combinations is publicly available on Zenodo (Fetzer, 2023b).

	Shielding Layers					**Ionising dose [krad]**		
Rank	**A**	**B**	**C**	**D**	**E**	**Electrons**	**Protons**	**Total Dose**
1	PE	PE	PE	PE	W	0.1809 ± 0.0017	0.3341 ± 0.0014	0.5149 ± 0.0022
2	PE	PE	PE	W	W	0.1362 ± 0.0015	0.3857 ± 0.0014	0.522 ± 0.0021
3	PE	PE	W	PE	W	0.1454 ± 0.0016	0.3811 ± 0.0017	0.5265 ± 0.0023
4	PE	PE	PE	FR4	W	0.1863 ± 0.0018	0.3519 ± 0.0013	0.5381 ± 0.0022
5	PE	PE	FR4	PE	W	0.1879 ± 0.0018	0.3513 ± 0.0012	0.5392 ± 0.0021
...	...	...	...	...	...	...	...	...
1012	Al-7075	Al-7075	Al-7075	Al-7075	Al-7075	0.5246 ± 0.0028	0.4089 ± 0.001	0.934 ± 0.0032
...	...	...	...	...	...	...	...	...
1020	W	Al-7075	Al-7075	Al-7075	FR4	0.5302 ± 0.0026	0.4278 ± 0.001	0.958 ± 0.003
1021	W	W	W	W	W	0.2501 ± 0.0018	0.71 ± 0.002	0.96 ± 0.0025
1022	W	FR4	Al-7075	Al-7075	Al-7075	0.527 ± 0.0027	0.4333 ± 0.002	0.96 ± 0.0031
1023	W	Al-7075	Al-7075	FR4	Al-7075	0.5288 ± 0.0027	0.432 ± 0.002	0.961 ± 0.0031
1024	W	Al-7075	Al-7075	Al-7075	Al-7075	0.5467 ± 0.0028	0.4413 ± 0.001	0.988 ± 0.0031

tion 2.5. This was performed for both two-layer and three-layer shields.

3.3.1. Two-layer mass allocation optimisation

Fig. 10 shows the total dose received in a 0.5 mm silicon plate behind 1.5 g/cm^2 of polyethylene on top of lead shielding with the trapped electron and proton spectra as described in Section 2.1.

The x-axis shows the mass allocation to polyethylene, with the remainder of the mass being lead. The simulation was performed for both polyethylene on top of lead and lead on top of polyethylene. The resulting TID is non-linear dependent on the mass allocation and the order of the materials. The data for polyethylene on top of lead shows a clear optimum between 70% to 80% of the 1.5 g/cm^2 being allocated to polyethylene, with the lowest TID being significantly lower than for shielding with purely one of the materials. If lead is on top of polyethylene, the TID can be up to 50% higher, highlighting the importance of the order of materials.

This non-linear dependency of the TID on the mass allocation was also observed in most of the other simulated material combinations, as shown in Fig. 11. The simulations suggest that for combinations of materials with significant differences in atomic mass number, the best shielding performance can be achieved with a combination of the two materials, which is better than shields that only contain one of the materials. For materials with similar atomic mass numbers, the TID minimum can be on the extreme ends of the mass allocation. In these cases, there is no benefit of having a second material since the best performance can be achieved by one of the two materials alone.

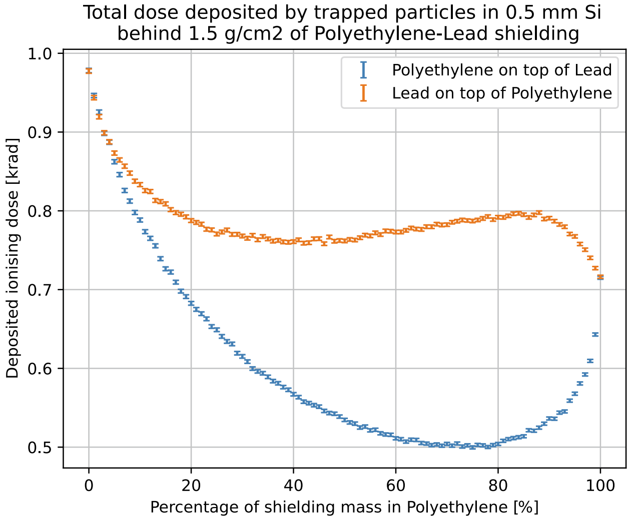

Fig. 10. Total dose behind polyethylene-lead shielding with varying ratio between the materials for constant 1.5 g/cm^2 shielding depth. The total dose depends on the mass ratio and the order of the materials.

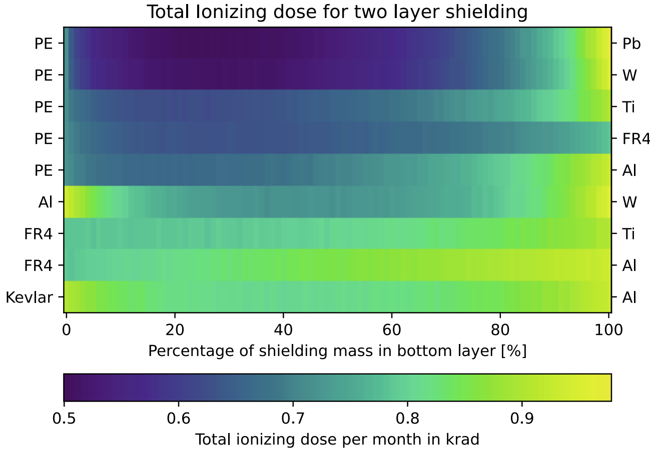

Fig. 11. Total dose received in 0.5 mm of silicon behind 1.5 g/cm^2 of two-layer shielding with varying mass allocation between the materials. The material labels on the left denote the top layers that face the incoming particles, while the labels on the right are the bottom layer materials.

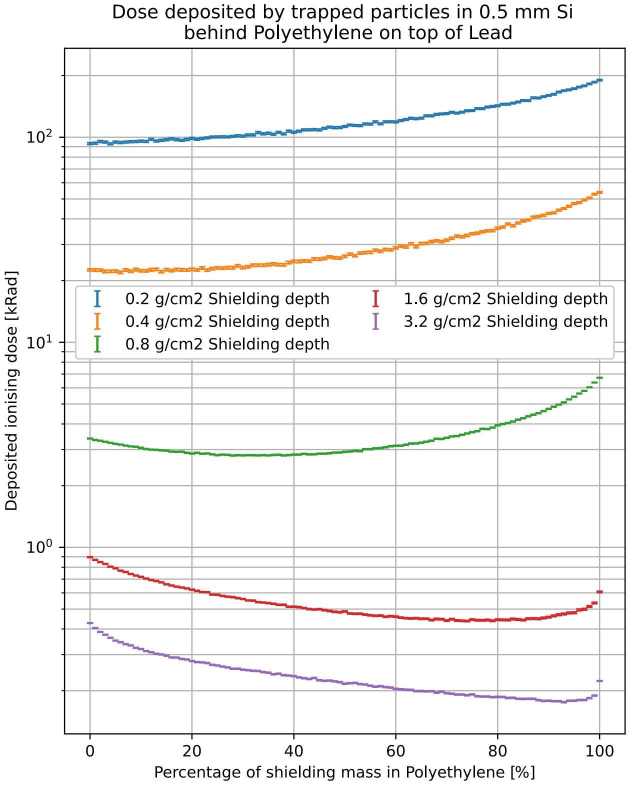

Fig. 12. Two-layer shields with varying mass allocations of polyethylene on top of lead for different shielding depths. The optimal composition depends on the total depth. For very thin shields, the lowest TID can be achieved with purely lead shielding, while the thickest shield achieves the lowest TID with more than 90% of the mass allocated to polyethylene.

3.3.2. Depth dependence of mass allocation optimisation

When varying the composition of a two-layer shield, the optimal material allocation depends on the particle spectra and the total depth of the shield.

Fig. 12 shows two-layer optimisation results for polyethylene on top of lead for five different total shielding depths. For 0.2 g/cm^2, the minimum TID result is close to 0% of the shielding mass in polyethylene. If the total shielding depth is limited to only 0.2 g/cm^2, a shield containing only lead would be the optimal solution. For 0.8 g/cm^2, the optimum lies between 30% and 40%, and the minimum is significantly lower than for the pure materials. For very thick shielding, the optimum is close to 100% polyethylene with only a thin lead layer in the back. If minimal dose rates are required, shielding with thick slabs of polyethylene would be a weight-efficient solution. Therefore, the trade-off to deciding a suitable shielding solution must consider what dose rates are acceptable and how much mass and volume can be allocated to the shielding. To allow for comparison between the results, all other simulations were performed with 1.5 g/cm^2 as discussed in Section 3.1.

3.3.3. Three-layer mass allocation optimisation

The layer mass allocation optimisation can be generalised to three layers, as explained in Section 2.6.

Fig. 13 shows the ionising dose due to trapped electrons received behind three-layer shields of varying composition, with the top layer being polyethylene, the second layer being aluminium, and the last layer being lead. The best combination is located on the edge of the ternary plane between lead and polyethylene, which means the best two-layer combination of polyethylene and lead performed better than any combination that contains aluminium between the polyethylene and lead layers.

The geometry of Fig. 13 was also simulated with the trapped proton spectrum, as shown in Fig. 14. For protons, the tile with the lowest dose contains only polyethylene.

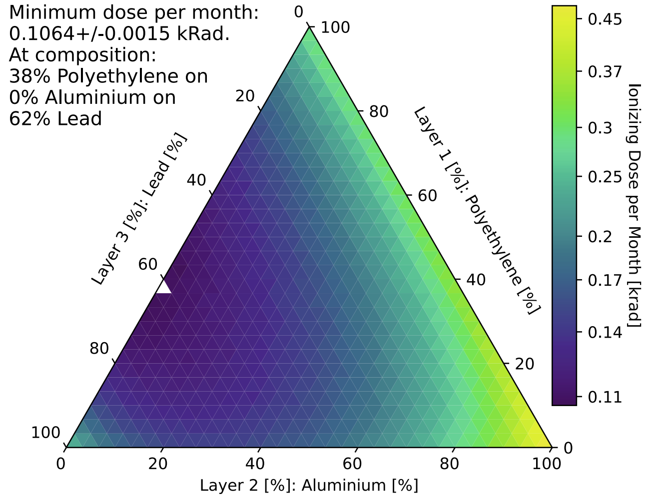

Fig. 13. Ionising dose due to trapped electrons received in 0.5 mm of silicon behind 1.5 g/cm^2 of three-layer polyethylene-aluminium-lead shielding with varying mass allocation between the materials. The tile with the lowest TID is highlighted in white.

This means a proton shield would not benefit from adding either aluminium or lead behind polyethylene.

Fig. 15 shows the dependence of total dose on the mass allocation between the layers for polyethylene on top of aluminium and lead. The optimum is located on the edge of the ternary plane between the polyethylene and lead corners, which means the optimised shield contains only two of the materials. Similar patterns were observed for all other simulated three-layer combinations. The results of the other simulations are summarised in Table 5.

Every row in Table 5 contains one material with zero percent of the shielding depth allocated to it. This means all the presented three-layer combinations could be optimised by removing one of the materials. This is further evidence that for the given particle spectra and investigated materials, there is no benefit for more than two layers.

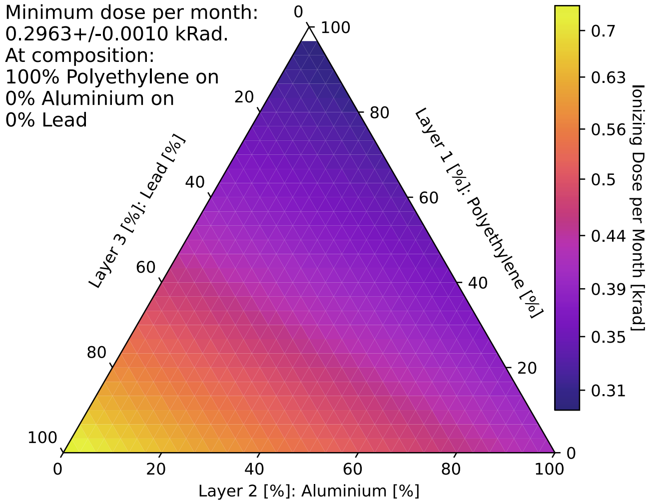

Fig. 14. Ionising dose due to trapped protons received in 0.5 mm of silicon behind 1.5 g/cm^2 of three-layer polyethylene-aluminium-lead shielding with varying mass allocation between the materials. The tile with the lowest TID is highlighted in white.

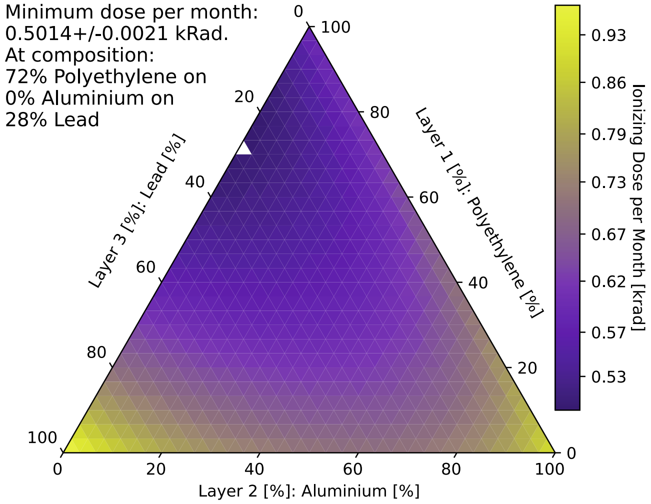

Fig. 15. Total dose due to trapped particles received in 0.5 mm of silicon behind 1.5 g/cm^2 of three-layer shielding with varying mass allocation between the materials. The tile with the lowest TID is highlighted in white.

Table 5
Summary of the optimisation results for three-layer radiation shields. The configuration that yielded the lowest TID for the three materials is presented, along with the corresponding percentage contribution of each material to the total shielding mass. The resulting TID is reported in krad, including statistical error.

Optimised material composition			Total dose
Layer A	**Layer B**	**Layer C**	**[krad]**
76 % PE	0 % W	24 % Pb	0.5000 ± 0.0022
72 % PE	0 % Al	28 % Pb	0.5014 ± 0.0021
72 % PE	28 % W	0 % PE	0.5066 ± 0.0021
0 % Al	76 % PE	24 % W	0.5102 ± 0.0022
0 % W	79 % PE	21 % W	0.5110 ± 0.0022
69 % PE	0 % Al	31 % W	0.5118 ± 0.0020
76 % PE	0 % Al	24 % FR4	0.6261 ± 0.0027
0 % Al	66 % FR4	34 % W	0.6555 ± 0.0024
0 % FR4	83 % PE	17 % Al	0.6798 ± 0.0028
0 % Al	86 % PE	14 % Al	0.6808 ± 0.0027
48 % Al	52 % W	0 % Al	0.7043 ± 0.0024
0 % Al	100 % FR4	0 % Al	0.7891 ± 0.0030

4. Conclusion and outlook

The shielding simulations presented in this article aimed to identify material combinations and layer structures that minimise the ionising dose received inside small satellites on missions to Earth's radiation belts.

The Geant4 simulation toolkit was used with the GRAS application to compute the interaction of trapped particle spectra with various shielding materials arranged in multilayer configurations with up to five layers.

The results show that the total ionising dose received in silicon plates behind multilayer shielding is non-linearly dependent on the mass allocation between different materials in two- and three-layer shielding configurations. This indicates that optimising the mass allocation in multilayer shielding systems can lead to significantly lower TID than single-material shielding systems of the same total mass. Optimised polyethylene-lead shields achieved up to 30% lower ionising doses compared to an equal mass of either of the two materials or up to 50% lower than the same mass of aluminium. Especially for CubeSats which have constrained mass budgets and a tendency to fail prematurely, this can mean mission extensions by several months or several hundred grams in mass savings (Poghosyan and Golkar, 2017).

The configurations which resulted in the lowest TID behind 1.5 g/cm^2 deep shielding consistently combined low-Z materials, such as polyethylene, in the top layers with high-Z materials, such as tungsten, lead or tantalum, in the bottom layers. Configurations with low-Z materials in the final layer performed poorly in all the presented simulations. Notably, the TID values did not show significant reductions when increasing the number of layers in the shielding configurations beyond two layers. The most effective two-layer configurations performed similarly to the best configurations with up to five layers. This finding suggests that, within the constraints of this article, dividing the shielding mass into more than two layers of different materials may not lead to an improvement in shielding performance against the trapped particles of Earth's radiation belts.

This seems to contradict claims about Z-graded shielding such as made by Fan et al. (Fan et al., 1996) and Wrobel et al. (Wrobel et al., 2013), who proposed three-layer shielding with a low-Z top layer, high-Z core and low-Z final layer. Other examples of multilayer shielding with three or more layers in the literature are given by Han et al. (Han et al., 2023), Gohel and Makwana (Gohel and Makwana, 2022), Sazali et al. (Arif Sazali et al., 2019) and Yang et al. (Yang et al., 2015). On the other hand, the older two-layer optimisation results of Rossi et al. (Rossi and Stauber, 1977) and Barnea et al. (Barnea et al., 1987) are supported by the presented results.

It is important to note that the simulation results are specific to the 1.5 g/cm^2 shielding depth and trapped particle spectra considered in this article. The trapped particle spectra were used merely as an example environment to demonstrate the optimisation methods, which could be applied to any particle type and spectra covered by the Geant4 physics models. Further simulations with different shielding depths, materials, and other radiation environments may yield different results. Additionally, other factors, such as structural integrity, weight, and cost, should be considered when selecting shielding materials and designing radiation protection systems for nanosatellites and other spacecraft. The optimisation only focused on the total ionising dose. Displacement damage and single-event effects should also be considered when designing a satellite but these effects require different shielding and mitigation strategies that are outside the scope of this study (Zheng et al., 2019). The results presented in this article are based purely on Monte Carlo particle transport simulations with the FTFP_BERT physics model. Validation attempts have been made as part of this study by comparing results from FTFP_BERT with SHIELDOSE-2Q and other Geant4 physics models and good agreement has been found, but alternative models might yield higher accuracy or better performance. Particle transport simulations must also be supported by measurements at accelerator facilities and in the actual trapped particle radiation environment in space. The Foresail-2 mission is proposed to perform such measurements on GTO using a dedicated radiation and shielding instrument, currently under development at Aalto University under the name RadEx (Fetzer et al., 2023; Anger et al., 2023).

In conclusion, if multilayer shielding is used, it must be optimised for the specific radiation environment and the specific requirements of the spacecraft or mission. The proposed multilayer optimisation methods are therefore the main result of this article. We encourage the reader to use these methods to optimise their own multilayer radiation shielding for the specific radiation environment of their mission.

Declaration of generative AI and AI-assisted technologies in the writing process

While preparing this work, the authors used GPT-4 by OpenAI to proofread and improve the language of the article. After using this tool, the authors reviewed and edited the content as needed and take full responsibility for the content of the publication.

Declaration of Competing Interest

The authors declare that they have no known competing financial interests or personal relationships that could have appeared to influence the work reported in this paper.

Acknowledgements

All simulations for this article were performed using the Aalto University Triton computing cluster provided by the Aalto Science-IT project. The research presented in this article was performed as part of and financed by the Finnish Centre of Excellence in Research of Sustainable Space (FORESAIL), a project under the Research Council of Finland decision numbers 312358 and 336808.

References

Aalto Science-IT, 2022. Cluster overview: Shared resource. URL: https://scicomp.aalto.fi/triton/overview/.

Agostinelli, S., Allison, J., Amako, K., et al., 2003. Geant4-a simulation toolkit. Nucl. Instrum. Methods Phys. Res., Sect. A 506 (3), 250–303. https://doi.org/10.1016/S0168-9002(03)01368-8.

Allison, J., Amako, K., Apostolakis, J., et al., 2006. Geant4 developments and applications. IEEE Trans. Nucl. Sci. 53 (1), 270–278. https://doi.org/10.1109/tns.2006.869826.

Allison, J., Amako, K., Apostolakis, J., et al., 2016. Recent developments in Geant4. Nucl. Instrum. Methods Phys. Res., Sect. A 835, 186–225. https://doi.org/10.1016/j.nima.2016.06.125.

Anger, M., Fetzer, A., Janes, N. et al., 2022. FORESAIL-2: System engineering challenges for CubeSat missions in high radiation orbits. In: The 4S Symposium 2022. URL: https://az659834.vo.msecnd.net/eventsairwesteuprod/production-atpi-public/bb0fee8fd4c344538fb9500505a905e6.

Anger, M., Niemelä, P., Cheremetiev, K., et al., 2023. Foresail-2: Space Physics Mission in a Challenging Environment. Space Sci Rev 219, 66. https://doi.org/10.1007/s11214-023-01012-7.

Anil Kumar, V., Gupta, R., Prasad, M., et al., 2021. Recent advances in processing of titanium alloys and titanium aluminides for space applications: A review. J. Mater. Res. 36, 689–716. https://doi.org/10.1557/s43578-021-00104-w.

Arif Sazali, M., Alang Md Rashid, N.K., Hamzah, K., 2019. A review on multilayer radiation shielding. IOP Conf. Ser.: Mater. Sci. Eng. 555 (1). https://doi.org/10.1088/1757-899x/555/1/012008.

Badhwar, G., O'Neill, P., 1996. Galactic cosmic radiation model and its applications. Adv. Space Res., 17(2), 7–17. https://doi.org/10.1016/0273-1177(95)00507-B. Proceedings of the Meetings F2.6 and F2.7 of COSPAR Scientific Commission F which was held during the Thirtieth COSPAR Scientific Assembly.

Banerjee, S., 2012. CMS Simulation Software. J. Phys: Conf. Ser. 396 (2). https://doi.org/10.1088/1742-6596/396/2/022003.

Barnea, G., Berger, M.J., Seltzer, S.M., 1987. Optimization study of electron-bremsstrahlung shielding for manned spacecraft. J. Spacecr. Rock. 24 (2), 158–161. https://doi.org/10.2514/3.25889.

Blum, L.W., Kepko, L., Turner, D. et al., 2020. The GTOSat CubeSat: scientific objectives and instrumentation. In: George, T., Islam, M.S. (Eds.), Micro- and Nanotechnology Sensors, Systems, and Applications XII, vol. 11389, International Society for Optics and Photonics Spie, pp. 62–71, https://doi.org/10.1117/12.2556268.

Cern, 2020. GDML users's guide: Version 2.8. URL: https://gdml.web.cern.ch/GDML/doc/GDMLmanual.pdf.

Chytracek, R., Mccormick, J., Pokorski, W., et al., 2006. Geometry description markup language for physics simulation and analysis applications. IEEE Trans. Nucl. Sci. 53 (5), 2892–2896. https://doi.org/10.1109/tns.2006.881062.

Daneshvar, H., Milan, K.G., Sadr, A., et al., 2021. Multilayer radiation shield for satellite electronic components protection. Sci. Rep. 11 (1), 20657. https://doi.org/10.1038/s41598-021-99739-2.

Donder, E.D., Messios, N., Calders, S. et al., 04.05.2018. SPace ENVironment Information System: SPENVIS. URL: https://www.spenvis.oma.be/.

Elsaesser, A., Merenda, F., Lindner, R., et al., 2020. SpectroCube: a European 6U nanosatellite spectroscopy platform for astrobiology and astrochemistry. Acta Astronaut. 170, 275–288. https://doi.org/10.1016/j.actaastro.2020.01.028.

Emmanuel, A., Raghavan, J., 2015. Influence of structure on radiation shielding effectiveness of graphite fiber reinforced polyethylene composite. Adv. Space Res. 56 (7), 1288–1296. https://doi.org/10.1016/j.asr.2015.06.028.

Emmanuel, A., Raghavan, J., 2016. Experimental validation of simulations of radiation shielding effectiveness of materials by mulassis. Adv. Space Res. 58 (11), 2376–2384. https://doi.org/10.1016/j.asr.2016.08.018.

Emmanuel, A., Raghavan, J., Harris, R., et al., 2014. A comparison of radiation shielding effectiveness of materials for highly elliptical orbits. Adv. Space Res. 53 (7), 1143–1152. https://doi.org/10.1016/j.asr.2013.12.039.

Everett, M., Flores-Abad, A., Khan, A. et al., 2018. A 1U cube-satellite for electrically conductive 3D printing in GTO. In: 2018 AIAA SPACE and Astronautics Forum and Exposition. https://doi.org/10.2514/6.2018-5231.

Fan, W.C., Drumm, C.R., Roeske, S.B., et al., 1996. Shielding considerations for satellite microelectronics. IEEE Trans. Nucl. Sci. 43 (6), 2790–2796. https://doi.org/10.1109/23.556868.

Fetzer, A., 2023a. Shielding performance of the 98 first chemical elements against trapped particles on GTO. https://doi.org/10.5281/zenodo.7616012.

Fetzer, A., 2023b. Simulated shielding performance of 1024 five-layer permutations of four satellite and radiation shielding materials against trapped particles on GTO. https://doi.org/10.5281/zenodo.7622159.

Fetzer, A., 2023c. Simulated shielding performance of 1296 four-layer permutations of six common satellite and radiation shielding materials against trapped particles on GTO. https://doi.org/10.5281/zenodo.7621281.

Fetzer, A., 2023d. Simulated shielding performance of 1728 three-layer permutations of 12 common satellite and radiation shielding materials against trapped particles on GTO. https://doi.org/10.5281/zenodo.7620703.

Fetzer, A., 2023e. Simulated shielding performance of 2500 two-layer permutations of the first 50 chemical elements against trapped particles on GTO. https://doi.org/10.5281/zenodo.7828929.

Fetzer, A., Anger, M., Kärkkäinen, T. et al., 2023. Radiation shielding experiment for cubesat on highly elliptical orbit. URL: https://research.aalto.fi/en/publications/radiation-shielding-experiment-for-cubesat-on-highly-elliptical-o abstract and presentation at the Space Environment Monitoring Workshop (SPACEMON), Conference date: 15-05-2023 Through 17-05-2023.

Freeman, A., 2020. Exploring our solar system with CubeSats and SmallSats: the dawn of a new era. CEAS Space J. 12 (4), 491–502. https://doi.org/10.1007/s12567-020-00298-5.

Geant4 Collaboration, 2021. Geant4 material database. URL: https://geant4-userdoc.web.cern.ch/UsersGuides/ForApplicationDeveloper/html/Appendix/materialNames.html.

Geant4 collaboration, 2022. Geant4: A simulation toolkit. URL: https://geant4.web.cern.ch/.

Geant4 Collaboration, 2023a. Geant4 Physics Reference Manual. CERN. URL: https://geant4.web.cern.ch/docs/#physics-reference-manual Release 11.1, Rev7.1: July 31st, 2023.

Geant4 Collaboration, 2023b. Guide for physics lists. URL: https://geant4.web.cern.ch/docs/#physics-list-guide rev7.1: July 31st, 2023.

Ginet, G.P., O'Brien, T.P., Huston, S.L., et al., 2013. AE9, AP9 and SPM: New models for specifying the trapped energetic particle and space plasma environment. Space Sci. Rev. 179 (1–4), 579–615. https://doi.org/10.1007/s11214-013-9964-y.

Gohel, A., Makwana, R., 2022. Multi-layered shielding materials for high energy space radiation. Radiat. Phys. Chem. 197, 110131. https://doi.org/10.1016/j.radphyschem.2022.110131.

Han, Z.-W., Song, K.-F., Liu, S.-J., et al., 2023. Lightweight omnidirectional radiation protection for a photon-counting imaging system in space applications. Appl. Sci. 13 (10). https://doi.org/10.3390/app13105905.

Heynderickx, D., Quaghebeur, B., Speelman, E. et al., 2000. ESA's SPace ENVironment Information System (SPENVIS)-A WWW interface to models of the space environment and its effects. In: 38th Aerospace Sciences Meeting and Exhibit, p. 371. https://doi.org/10.2514/6.2000-371.

Heynderickx, D., Quaghebeur, B., Wera, J., et al., 2004. New radiation environment and effects models in the European Space Agency's SPace ENVironment Information System (SPENVIS). Space Weather 2 (10). https://doi.org/10.1029/2004sw000073.

Heynderickx, D., Quaghebeur, B., Wera, J. et al., 2005. ESA's SPace ENVironment Information System (SPENVIS): A web-based tool for assessing radiation doses and effects in spacecraft systems. In: Proceedings of the Space Nuclear Conference 2005. URL: https://orfeo.belnet.be/handle/internal/4602.

Hu, H., Wang, Q., Qin, J., et al., 2008. Study on composite material for shielding mixed neutron and gamma rays. IEEE Trans. Nucl. Sci. 55 (4), 2376–2384. https://doi.org/10.1109/TNS.2008.2000800.

Ibarmia, S., Eck, J., Ivanchenko, V., et al., 2013. Experimental dose enhancement in multi-layer shielding structures exposed to high-energy electron environments. IEEE Trans. Nucl. Sci. 60 (4), 2486–2493. https://doi.org/10.1109/tns.2013.2273087.

International Organization for Standardization, 2004. ISO 15390:2004, Space environment (natural and artificial) - galactic cosmic ray model. Standard Iso 15390:2004 International Organization for Standardization. URL: https://www.iso.org/standard/37095.html last reviewed and confirmed in 2018.

Rípa, J., Dilillo, G., Campana, R. et al., 2020. A comparison of trapped particle models in low Earth orbit. In: den Herder, J.-W.A., Nikzad, S., Nakazawa, K. (Eds.), Space Telescopes and Instrumentation 2020: Ultraviolet to Gamma Ray. vol. 11444. International Society for Optics and Photonics SPIE, p. 114443P. https://doi.org/10.1117/12.2561011.

Ivantchenko, A.V., Ivanchenko, V.N., Molina, J.-M.Q., et al., 2012. Geant4 hadronic physics for space radiation environment. Int. J. Radiat. Biol. 88 (1–2), 171–175. https://doi.org/10.3109/09553002.2011.610865.

Jiggens, P., Varotsou, A., Truscott, P., et al., 2018. The solar accumulated and peak proton and heavy ion radiation environment (SAPPHIRE) model. IEEE Trans. Nucl. Sci. 65 (2), 698–711. https://doi.org/10.1109/tns.2017.2786581.

Jiggens, Piers, Chavy-Macdonald, Marc-Andre, Santin, Giovanni, et al., 2014. The magnitude and effects of extreme solar particle events. J. Space Weather Space Clim. 4 (A20). https://doi.org/10.1051/swsc/2014017.

Klamm, B., 2015. Passive space radiation shielding: Mass and volume optimization of tungsten-doped polyphenolic and polyethylene resins. In: Proceedings of the 29th Annual AIAA/USU Conference on Small Satellites. URL: https://digitalcommons.usu.edu/smallsat/2015/all2015/24/.

Kopacz, J.R., Herschitz, R., Roney, J., 2020. Small satellites an overview and assessment. Acta Astronaut. 170, 93–105. https://doi.org/10.1016/j.actaastro.2020.01.034.

Lei, F., Truscott, R.R., Dyer, C.S., et al., 2002. MULASSIS: a Geant4-based multilayered shielding simulation tool. IEEE Trans. Nucl. Sci. 49 (6), 2788–2793. https://doi.org/10.1109/tns.2002.805351.

Lucas, J., Grubb, M., Morris, J. et al., 2022. GTOSat: Radiation Belt Dynamics from the Inside. In: Proceedings of the Small Satellite Conference. URL: https://digitalcommons.usu.edu/smallsat/2022/all2022/145/.

Madry, S., Pelton, J.N., 2020. Historical perspectives on the evolution of small satellites. In: Handbook of Small Satellites: Technology, Design, Manufacture, Applications, Economics and Regulation. Springer International Publishing, pp. 33–48. https://doi.org/10.1007/978-3-030-36308-6_2.

Martins, M., Gomes, R., Pina, L., et al., 2018. Highly conductive carbon fiber-reinforced polymer composite electronic box: Out-of-autoclave manufacturing for space applications. Fibers 6 (4), 92. https://doi.org/10.3390/fib6040092.

Mewaldt, R.A., 2007. Solar energetic particle composition, energy spectra, and space weather. Space Sci. Rev. 124 (1–4), 303–316. https://doi.org/10.1007/s11214-006-9091-0.

Narici, L., Casolino, M., Di Fino, L., et al., 2017. Performances of kevlar and polyethylene as radiation shielding on-board the international space station in high latitude radiation environment. Sci. Rep. 7 (1), 1644. https://doi.org/10.1038/s41598-017-01707-2.

Poghosyan, A., Golkar, A., 2017. Cubesat evolution: Analyzing cubesat capabilities for conducting science missions. Prog. Aerosp. Sci. 88, 59–83. https://doi.org/10.1016/j.paerosci.2016.11.002.

Rohach, A.F., 1966. Weight optimization of gamma-ray shields using layered media and spherical geometry. Nucl. Sci. Eng. 27 (2), 464–466. https://doi.org/10.13182/nse67-a18285.

Rossi, M., Stauber, M., 1977. Radiation protection design considerations for man in geosynchronous orbits. IEEE Trans. Nucl. Sci. 24 (6), 2248–2251.

Russell, C., 2000. The solar wind interaction with the Earth's magnetosphere: A tutorial. IEEE Trans. Plasma Sci. 28 (6), 1818–1830. https://doi.org/10.1109/27.902211.

Rutledge, S.K., Banks, B.A., Kitral, M., 2001. A comparison of space- and ground-based facility environmental effects for Fep Teflon. In: Protection of Materials and Structures from the Low Earth Orbit Space Environment, pp. 165–179. https://doi.org/10.1007/978-94-010-0714-6_13.

Samwel, S.W., El-Aziz, E.A., Garrett, H.B., et al., 2019. Space radiation impact on smallsats during maximum and minimum solar activity. Adv. Space Res. 64 (1), 239–251. https://doi.org/10.1016/j.asr.2019.03.025.

Santin, G., Ivanchenko, V., Evans, H., et al., 2005. GRAS: a general-purpose 3-D modular simulation tool for space environment effects analysis. IEEE Trans. Nucl. Sci. 52 (6), 2294–2299. https://doi.org/10.1109/tns.2005.860749.

Sasse, S., 1965. Method for weight optimization of a two-material shield for reactor radiation. Nucl. Struct. Eng. 2 (3), 327–334. https://doi.org/10.1016/0369-5816(65)90090-6.

Scoles, S., 2022. Prime mover. Science 377 (6607), 702–705. https://doi.org/10.1126/science.ade2873.

Seltzer, S.M., 1980. SHIELDOSE: a computer code for Space-Shielding Radiation Dose Calculations. Final report. Department of Commerce, National Bureau of Standards. URL: https://www.osti.gov/biblio/6675823. https://doi.org/10.6028/NBS.TN.1116 NBS Technical Note 1116.

Seltzer, S.M., 1994. Updated calculations for routine space-shielding radiation dose estimates: SHIELDOSE-2. NIST Pubs, URL: https://ntrl.ntis.gov/NTRL/dashboard/searchResults/titleDetail/PB95171039.xhtml.

Spenvis, 2018. Ionising dose model SHIELDOSE. URL: https://www.spenvis.oma.be/help/background/shieldose/shieldose.html.

The Aluminum Association, 2018. International alloy designations and chemical composition limits for wrought aluminum and wrought aluminum alloys. URL.

The CubeSat Program, 2022. CubeSat design specification. URL: https://www.cubesat.org/cubesatinfo.

Thomsen, D., Kim, W., Cutler, J., 2015. Shields-1, A SmallSat radiation shielding technology demonstration. In: Proceedings of the Small Satellite Conference. URL: https://digitalcommons.usu.edu/smallsat/2015/all2015/84/.

Tykhonov, A., 2019. cad-to-geant4-converter: A light-weight tool for converting CAD drawings into the GDML format. URL: https://github.com/tihonav/cad-to-geant4-converter.

Vainio, R., Desorgher, L., Heynderickx, D., et al., 2009. Dynamics of the Earth's particle radiation environment. Space Sci. Rev. 147 (3–4), 187–231. https://doi.org/10.1007/s11214-009-9496-7.

Winokur, P.S., Lum, G.K., Shaneyfelt, M.R., et al., 1999. Use of COTS microelectronics in radiation environments. IEEE Trans. Nucl. Sci. (Inst. Electr. Electron. Eng.) 46 (6Pt1). https://doi.org/10.1109/23.819113.

Woellert, K., Ehrenfreund, P., Ricco, A.J., et al., 2011. Cubesats: Cost-effective science and technology platforms for emerging and developing nations. Adv. Space Res. 47 (4), 663–684. https://doi.org/10.1016/j.asr.2010.10.009.

Workman, R.L., Others (Particle Data Group), 2022. Review of particle physics. PTEP, 2022, 083C01. https://doi.org/10.1093/ptep/ptac097.

Wrobel, J., Hoyt, R., Cushing, J. et al., 2013. Versatile structural radiation shielding and thermal insulation through additive manufacturing. In: Proceedings of the 27th Annual AIAA/USU Conference on Small Satellites. URL: https://digitalcommons.usu.edu/smallsat/2013/all2013/61/.

Yang, J., Ma, G., Li, X. et al., 2015. Effects of multilayer and multimaterial structures on space proton radiation protection. Nucl. Instrum. Methods Phys. Res. Sect. B: Beam Interact. Mater. Atoms, 365, 352–356. https://doi.org/10.1016/j.nimb.2015.08.054. Proceedings of the 19th International Conference on Ion Beam Modification of Materials (IBMM 2014).

Zheng, Y., Ganushkina, N., Jiggens, P., et al., 2019. Space radiation and plasma effects on satellites and aviation: Quantities and metrics for tracking performance of space weather environment models. Space Weather 17 (10), 1384–1403. https://doi.org/10.1029/2018SW002042.